University Library

MINERVA ACCESS

A gateway to Melbourne's research publications

Minerva Access is the Institutional Repository of The University of Melbourne

Author/s:
Alinejadtabrizi, T;Lang, F;Huang, Y;Ackermann, L;Keywood, M;Ayers, G;Krummel, P;Humphries, R;Williams, A;Siems, S;Manton, M

Title:
Wet deposition in shallow convection over the Southern Ocean

Date:
2024-02-27

Citation:
Alinejadtabrizi, T., Lang, F., Huang, Y., Ackermann, L., Keywood, M., Ayers, G., Krummel, P., Humphries, R., Williams, A., Siems, S. & Manton, M. (2024). Wet deposition in shallow convection over the Southern Ocean. npj Climate and Atmospheric Science, 7 (1), https://doi.org/10.1038/s41612-024-00625-1.

Persistent Link:
https://hdl.handle.net/11343/345530

License:
CC BY

npj | climate and atmospheric science

Article

Published in partnership with CECCR at King Abdulaziz University

https://doi.org/10.1038/s41612-024-00625-1

Wet deposition in shallow convection over the Southern Ocean

Check for updates

T. Alinejadtabrizi[1,2,3] ✉, F. Lang[1,4], Y. Huang[3,5], L. Ackermann[6], M. Keywood[7,8], G. Ayers[9], P. Krummel[7], R. Humphries[7,8], A. G. Williams[10], S. T. Siems[1,2] & M. Manton[1]

Southern Ocean (SO) air is amongst the most pristine on Earth, particularly during winter. Historically, there has been a focus on biogenic sources as an explanation for the seasonal cycle in cloud condensation nuclei concentrations (N_{CCN}). N_{CCN} is also sensitive to the strength of sink terms, although the magnitude of this term varies considerably. Wet deposition, a process encompassing coalescence scavenging (drizzle formation), is one such process that may be especially relevant over the SO. Using a boundary layer cloud climatology, N_{CCN} and precipitation observations from Kennaook/Cape Grim Observatory (CGO), we find a statistically significant difference in N_{CCN} between when the upwind meteorology is dominated by open mesoscale cellular convection (MCC) and closed MCC. When open MCC is dominant, a lower median N_{CCN} (69 cm^{-3}) is found compared to when closed MCC (89 cm^{-3}) is dominant. Open MCC is found to precipitate more heavily (1.72 mm day^{-1}) and more frequently (16.7% of the time) than closed MCC (0.29 mm day^{-1}, 4.5%). These relationships are observed to hold across the seasonal cycle with maximum N_{CCN} and minimum precipitation observed during Austral summer (DJF). Furthermore, the observed MCC morphology strongly depends on meteorological conditions. The relationship between N_{CCN} and precipitation can be further examined across a diurnal cycle during the summer season. Although there was again a negative relationship between precipitation and N_{CCN}, the precipitation cycle was out of phase with the N_{CCN} cycle, leading it by ~3 hours, suggesting other factors, specifically the meteorology play a primary role in influencing precipitation.

The atmosphere over the Southern Ocean (SO) is renowned for being the most pristine on Earth[1,2], since it is largely free of anthropogenic and terrestrial emissions. It is further renowned for its high fractional cloud cover[3] and high precipitation frequency[4] throughout the year, an immediate consequence of the strong latent heat flux that arises along the SO storm track. When these elements are combined, the SO can serve as a proxy for a pre-industrial environment, providing a natural testbed for aerosol-cloud-precipitation interactions (ACPI)[5–7]. Yet the limited understanding of SO clouds results in radiation budget biases in both reanalysis products and climate simulations[8–14].

These persistent biases have garnered extensive attention from the scientific community with numerous international field campaigns undertaken[15–17]. Many of these efforts have focused on better categorizing the sources and magnitude of cloud condensation nuclei (CCN) and ice nucleating particles (INP) given their effect on cloud microphysical properties[18].

For many years, dimethylsulfide (DMS), which is formed by planktonic algae in sea water and oxidizes in the atmosphere to make sulfate aerosol, has been thought to be the main source of CCN over the oceans[19–21]. First published more than three decades ago, the 'CLAW' hypothesis, an

[1]School of Earth, Atmosphere and Environment, Monash University, Melbourne, Victoria, Australia. [2]Australian Research Council Securing Antarctica's Environmental Future (SAEF), Melbourne, Victoria, Australia. [3]Australian Research Council Centre of Excellence for Climate Extremes (CLEX), Melbourne, Victoria, Australia. [4]Department of Geophysics, Universidad de Concepción, Concepción, Chile. [5]School of Geography, Earth and Atmospheric Sciences, The University of Melbourne, Melbourne, Victoria, Australia. [6]Australian Bureau of Meteorology, Melbourne, Victoria, Australia. [7]CSIRO Environment, Melbourne, Victoria, Australia. [8]Australian Antarctic Program Partnership, Institute for Marine and Antarctic Studies, University of Tasmania, Hobart, Tasmania, Australia. [9]Visiting Scientist Emeritus, Bureau of Meteorology, Melbourne, Victoria, Australia. [10]Environmental Research, ANSTO, Lucas Heights, New South Wales, Australia.
✉e-mail: tahereh.alinejadtabrizi@monash.edu

acronym from the first letters of the authors' surnames[19], defines a negative climate feedback loop between incident solar radiation, marine biogenic emissions, CCN and cloud properties, which has sparked sustained scientific interest. Many subsequent studies have confirmed specifics of the connections between oceanic phytoplankton and DMS emission to the atmosphere (e.g.[22]), and the relation of DMS-derived aerosol mass, CCN number concentrations (N_{CCN}) and various cloud properties like cloud droplet number and cloud optical properties (e.g.[23–27]).

Although several links in the suggested loop between cloud albedo, CCN, DMS, and phytoplankton have been confirmed, there has not yet been a comprehensive scientific synthesis of it on a worldwide basis[21]. Quinn and Bates[28] examined observations of the individual steps of this loop and concluded that the sources of CCN over the marine atmospheric boundary layer (MABL) are more complex than previously recognized and there should be other sinks and sources than DMS, especially during winter[26,29]. Later research focused less on DMS and more on other CCN sources. Leck and Bigg[30] illustrated that bubble bursting at the ocean surface is a significant source of CCN to the MABL, consistent with previous studies[31–33]. They demonstrated while a marine biological source of reduced sulfur dominates N_{CCN} over the summer months, other components, such as wind-generated coarse-mode sea salt, are important CCN components year-round, especially in winter due to higher winds[22,26,34–37].

Numerous recent research efforts have further underscored the importance of considering regionally varying meteorological factors for understanding ACPI[38–40]. For example, Zhang and Feingold[38], revealed the global distribution of marine low-cloud albedo susceptibility, emphasizing the strong influence of large-scale meteorological conditions on cloud albedo in various regions. They considered crucial factors such as lower-tropospheric stability, free-tropospheric relative humidity, sea surface temperature, and boundary layer depth, highlighting the need to account for these variables when assessing the response of cloud albedo to aerosol perturbations at different scales.

The removal of aerosols from the MABL by their activation into cloud droplets and subsequent development into precipitation-sized particles through collision-coalescence has long been acknowledged as a prominent mechanism addressing probable CCN sinks[7,41–43]. Recent research by Tornow et al.[44] demonstrated that frozen hydrometeors in marine cold air outbreaks can affect cloud liquid water and early consumption of CCN, leading to a reduction in cloud droplet number concentration (N_d). According to aircraft observations over the SO, Hudson found that CCN have lower concentrations in the MABL under cloudy conditions than clear conditions[2,45]. Also, the average N_d for wintertime flights with non-drizzling clouds is roughly three times higher than the overall average[45,46]. Bennartz[47] also used observations from the MODerate resolution Imaging Spectroradiometer (MODIS) to study the sensitivity of maritime clouds to precipitation and concluded that N_d was approximately 2.5 times greater in non-drizzling clouds than in drizzling clouds. In their idealized model of N_d for MABL clouds, Wood et al.[42] demonstrated that precipitation was the main sink of N_d. Using the same budget model, McCoy et al.[7] showed that coalescence scavenging might reduce the mean N_d to around 30% of the value that would occur otherwise. However, using a modified version of the same budget model, Kang et al.[43] found a reduction in anticipated N_d of up to 90% depending on the rate of precipitation. The impact of wet deposition, which is a direct aerosol removal process, is still poorly understood, especially over the SO, where great uncertainty exists in the amount and nature of precipitation[48–51].

MABL clouds, which are frequently shallow boundary-layer clouds, are the dominant cloud type over the SO[51–55]. Light precipitation from shallow clouds, on the other hand, has been found to be common over the SO as non-frontal precipitation[56–58]. According to satellite observations, MABL clouds frequently display some mesoscale morphological types, each of which is distinguished by certain patterns of cloud organization. Wood and Hartmann[59] categorized these clouds into open mesoscale cellular convection (MCC), closed MCC, no MCC, and cellular but disorganized clouds based on the mesoscale organization. The type of MCC introduces significant mesoscale variability in both the microphysical (e.g., N_d, effective radius, precipitation rate) and macrophysical (e.g., cloud albedo, cloud coverage) properties of clouds[59–63]. In-situ observations have found that drizzle/light precipitation is more frequent and intense in open MCCs, while closed cells have very few drizzle drops[43,46,64,65].

Building upon these field observations, we seek to quantify climatological differences in the relationships between cloud morphology, precipitation and their meteorological controls, and to extend this relationship to N_{CCN} as observed at the Kennaook/Cape Grim Observatory (CGO), Tasmania. This will be done by examining the sensitivity of N_{CCN} to precipitation from boundary layer clouds over the SO, considering the nature of the upwind shallow convection. The hypothesis is that "highly pristine conditions/low N_{CCN} over the SO are associated with periods of relatively high precipitation arising mainly from open MCC".

Results and discussion

CCN and precipitation relation within cloud morphology

From the 17,470 h of baseline data at CGO, the median N_{CCN} and mean precipitation are determined for samples with a specified upwind domain radius, upwind averaging time and the fraction of coverage for both open and closed MCC (FC_{MCC}) threshold. Tables 1, 2 show the results for the 50 and 80% FC_{MCC} threshold for both open and closed MCC, respectively. For each upwind radius and averaging time, the median N_{CCN} is shown along with the 5th and 95th percentiles; the number of samples is also indicated. The tables reveal that the results are robust across different upwind radii, averaging times, and FC_{MCC} thresholds.

The number of samples varies systematically with upwind radius and time. For an upwind averaging time of 3 h, for 80% FC_{MCC} threshold (Table 2), the maximum number of samples for open MCC (3403) occurs at an upwind radius of 200 km while the maximum for closed MCC (1050) occurs at a radius of 100 km. The number of samples depends upon the match between radius and time, accounting for the advection speed of cloud and the persistence of cloud type within the baseline sector. Qualitatively, the results are the same when the domain radius is set at 300 km or less. At larger radii the number of records drops steeply.

We assessed whether the examined properties of open and closed MCC (e.g., median N_{CCN} or mean precipitation rate and frequency) are different for each upwind radius and time, with the null hypothesis that any differences are only due to random variations. The analysis with the Whitney U test revealed statistically significant differences, with median N_{CCN} consistently smaller for open than closed MCC ($p < 0.05$). Similarly, the results of the two-tailed Student's t test confirmed that differences in precipitation rate and frequency between open and closed MCC are statistically significant ($p < 0.05$). As such for all results hereafter, we only consider the 100 km upwind average, 80% FC_{MCC} threshold (Table 2) for both open and closed and 3 h upwind averaging time, which gives a median N_{CCN} of 69 cm^{-3} from 3285 samples for open MCC and 89 cm^{-3} from 1050 samples for closed MCC. The precipitation rate for open MCC (1.72 mm day^{-1}) is 6 times greater than for closed MCC (0.29 mm day^{-1}) and the frequency of precipitation is also more frequent during open MCC, occurring 16.7% of the time compared to 4.5% for closed MCC. These results support the hypothesis that open MCC have higher precipitation than closed MCC, climatologically, which is consistent with previous field observations[46,66,67].

Figure 1a compares the probability distribution function (PDF) of N_{CCN} for open and closed MCC, while Fig. 1b compares the PDF of the precipitation. The precipitation from closed MCC is predominantly drizzle (less than 7.2 mm day^{-1} or 0.3 mm h^{-1}) rather than rain, with a frequency of 98.8% (orange solid line in Fig. 1b). Conversely, in the case of open MCC, drizzle accounts for precipitation 92.1% of the time (blue solid line in Fig. 1b). Figure 1a shows that very clean air with N_{CCN} less than 50 cm^{-3} is much more common under open MCC than closed MCC, suggesting that CCN could be washed out by wet deposition during the heavier rain under open MCC. Since both MCC types have similar modes within 50 to 100 cm^{-3}, the relative frequency of N_{CCN} higher than 100 cm^{-3} is lower for open than closed MCC. The bottom plots depict PDF of Mean Sea Level Pressure

https://doi.org/10.1038/s41612-024-00625-1

Table 1 | Median N_{CCN} and mean precipitation rate and frequency

Radius (km)-dominated MCC type	N_{CCN} (cm^{-3}) (5th, 95th) (No. of cases) 1 h	Precipitation intensity (mm day^{-1}), Frequency (%) 1 h	N_{CCN} (cm^{-3}) (5th, 95th) (No. of cases) 3 h	Precipitation intensity (mm day^{-1}), Frequency (%) 3 h	N_{CCN} (cm^{-3}) (5th, 95th) (No. of cases) 6 h	Precipitation intensity (mm day^{-1}), Frequency (%) 6 h
1000-Open MCC	85 (27, 211) (4273)	2.88, 19.6%	85 (27, 209) (4169)	2.64, 18.9%	85 (28, 207) (4057)	2.42, 17.9%
500-Open MCC	78 (24, 199) (5121)	2.72, 19.6%	78 (25, 199) (5045)	2.34, 18.3%	77 (24, 199) (4970)	2.01, 17.2%
300-Open MCC	74 (24, 193) (5136)	2.25, 18.3%	74 (24, 193) (5081)	1.98, 17.2%	74 (24, 193) (5013)	1.82, 16.1%
200-Open MCC	72 (23, 189) (5074)	1.98, 17.2%	72 (23, 189) (4997)	1.85, 16.7%	72 (23, 189) (4922)	1.78, 16.1%
100-Open MCC	71 (23, 183) (4710)	1.84, 16.6%	70 (23, 183) (4637)	1.79, 16.6%	70 (22, 183) (4546)	1.77, 16.3%
50-Open MCC	70 (23, 180) (4370)	1.77, 16.6%	69 (22, 180) (4331)	1.86, 16.9%	69 (22, 180) (4211)	1.88, 17.1%
1000-Closed MCC	88 (24, 207) (1010)	1.34, 11.2%	91 (25, 203) (952)	1.04, 9.9%	96 (26, 202) (877)	0.74, 8.2%
500-Closed MCC	91 (26, 236) (1855)	0.49, 6.7%	93 (25, 230) (1787)	0.49, 6.7%	93 (25, 228) (1640)	0.45, 6.2%
300-Closed MCC	91 (27, 242) (2047)	0.50, 6.9%	92 (29, 240) (1937)	0.44, 6.2%	93 (29, 235) (1822)	0.49, 6.1%
200-Closed MCC	91 (29, 242) (2039)	0.51, 7.1%	91 (30, 234) (1900)	0.44, 6.3%	91 (30, 222) (1721)	0.44, 5.9%
100-Closed MCC	91 (31, 231) (1894)	0.45, 6.6%	91 (32, 225) (1754)	0.41, 5.9%	91 (32, 219) (1597)	0.42, 5.1%
50-Closed MCC	91 (32, 226) (1726)	0.44, 6.6%	90 (32, 224) (1629)	0.44, 6.1%	90 (32, 221) (1453)	0.40, 4.7%

Results are for different upwind radii of baseline (different rows) and different averaging times (different columns) based on the 50% FC_{MCC} threshold for 2016–2021. The N_{CCN} columns contain the 5th and 95th percentiles and the number of cases in two separate brackets, respectively.

Table 2 | Median N_{CCN} and mean precipitation rate and frequency

Radius (km)-dominated MCC type	N_{CCN} (cm^{-3}) (5th, 95th) (No. of cases) 1 h	Precipitation intensity (mm day^{-1}), Frequency (%) 1 h	N_{CCN} (cm^{-3}) (5th, 95th) (No. of cases) 3 h	Precipitation intensity (mm day^{-1}), Frequency (%) 3 h	N_{CCN} (cm^{-3}) (5th, 95th) (No. of cases) 6 h	Precipitation intensity (mm day^{-1}), Frequency (%) 6 h
1000-Open MCC	87 (29, 207) (1335)	2.65, 19.0%	88 (30, 206) (1225)	2.27, 17.6%	88 (30, 206) (1074)	1.89, 15.2%
500-Open MCC	77 (25, 186) (2883)	2.23, 18.4%	77 (25, 183) (2677)	1.83, 17.0%	77 (25, 186) (2365)	1.63, 22.5%
300- Open MCC	74 (24, 184) (3441)	1.95, 17.4%	73 (24, 181) (3207)	1.71, 16.2%	72 (23, 179) (2867)	1.61, 15.6%
200-Open MCC	72 (23, 179) (3734)	1.82, 16.7%	71 (23, 178) (3403)	1.70, 16.3%	70 (22, 178) (2991)	1.60, 15.9%
100-Open MCC	70 (23,177) (3759)	1.80, 16.9%	69 (23, 174) (3285)	1.72, 16.7%	68 (22, 177) (2861)	1.64, 16.1%
50-Open MCC	69 (23, 176) (3679)	1.78, 16.8%	68 (23, 173) (3100)	1.74, 17.1%	67 (22, 173) (2666)	1.71, 16.4%
1000-Closed MCC	97 (30, 173) (93)	1.03, 9.7%	98 (36, 173) (79)	1.09, 11.4%	101 (41, 168) (58)	0.50, 6.9%
500-Closed MCC	88 (35, 238) (599)	0.39, 5.0%	89 (35, 228) (538)	0.32, 4.8%	91 (37, 224) (424)	0.18, 3.1%
300-Closed MCC	89 (35, 236) (953)	0.37, 5.5%	93 (36, 226) (824)	0.25, 3.6%	93 (37, 214) (672)	0.21, 3.3%
200-Closed MCC	91 (34, 229) (1152)	0.36, 5.3%	91 (35, 224) (969)	0.28, 4.1%	90 (35, 211) (765)	0.26, 3.7%
100-Closed MCC	88 (33, 229) (1296)	0.37, 5.6%	89 (34, 222) (1050)	0.29, 4.5%	86 (33, 211) (768)	0.28, 4.2%
50-Closed MCC	90 (33,225) (1312)	0.38, 6.0%	88 (34, 214) (976)	0.31, 4.7%	86 (32, 205) (690)	0.34, 5.1%

Results are for different upwind radii of baseline (different rows) and different averaging times (different columns) based on the 80% FC_{MCC} threshold for 2016–2021. The N_{CCN} columns contain the 5th and 95th percentiles and the number of cases in two separate brackets, respectively.

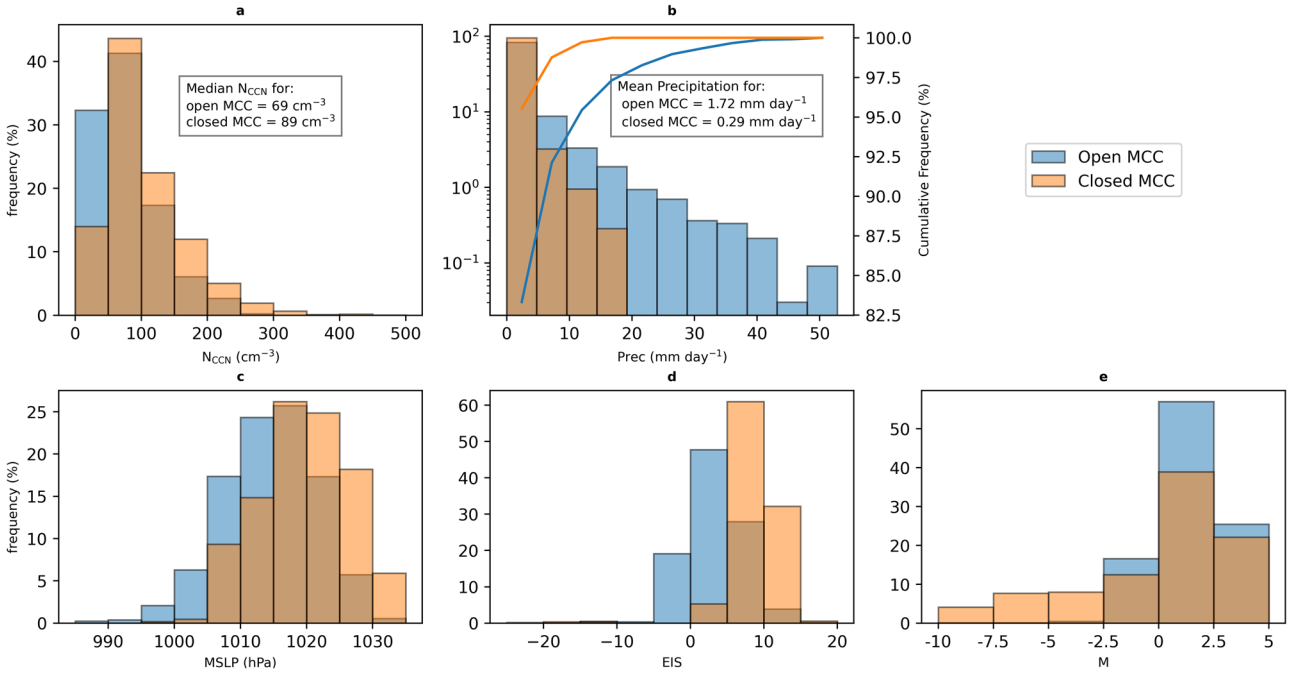


Fig. 1 | General atmospheric condition under different MCCs. Overlapping Probability Density Function (PDF) plot for N_{CCN} (**a**), PDF plot (left axis) and the accumulated frequency (solid lines-right axis) for the precipitation (**b**) and the PDF plot for MSLP (**c**), EIS (**d**) and M (**e**) in open (blue) and closed (orange) MCC conditions for the 100 km upwind radius and 3 h upwind averaging time and 80% FC_{MCC} threshold.

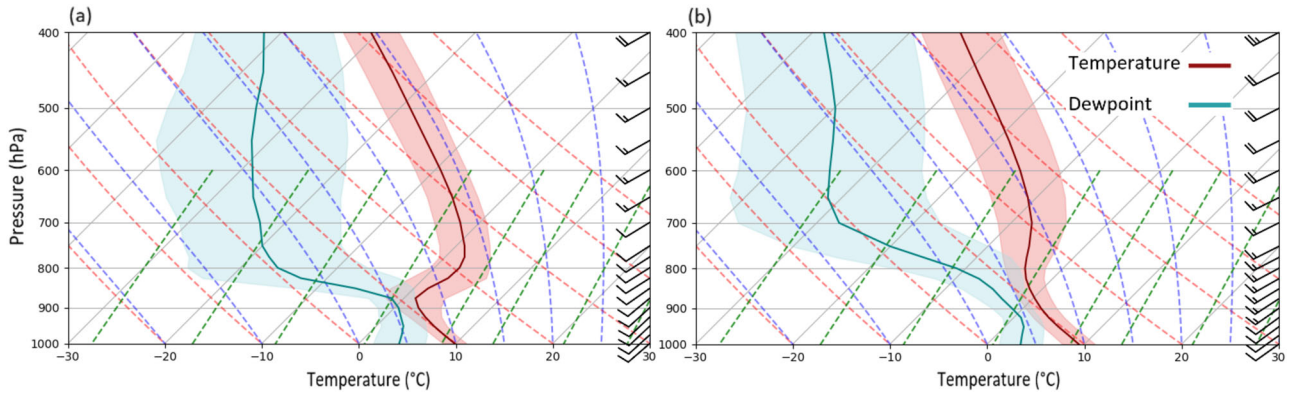


Fig. 2 | Composite soundings. Composite sounding profile for (**a**) closed MCC and (**b**) open MCC for the 100 km upwind radius and 3 h upwind averaging time and 80% FC_{MCC} threshold. Mean profiles of temperature (Red lines), dew point temperature (blue lines), and vector winds, shaded region indicates standard deviation.

(MSLP), the Estimated Inversion Strength (EIS) and M of both open and closed MCC from left to right respectively. These parameters offer insights into the meteorological controls operating under each condition. Analysis of these plots reveals a higher incidence of high-pressure systems during closed MCC, whereas open MCC tends to occur in regions with lower MSLP values (Fig. 1c). Lang et al.[68] presents observations from a recent field campaign illustrating the common post-frontal structure of the MCC upwind of CGO. Both stability parameters highlight a more stable condition for the closed MCC with a higher EIS and a lower M range (Fig. 1d, e), consistent with McCoy et al.[61]. Furthermore, statistical analysis, specifically the Kolmogorov–Smirnov (KS) test, was employed to test the null hypothesis that the distributions of these parameters are the same for open and closed MCC. The results confirmed significant differences in these distributions ($p < 0.05$), underscoring the distinct characteristics associated with each MCC type.

To further investigate the meteorological differences under open and closed MCC, we also examined their composite soundings using ERA5. As shown in Fig. 2, closed MCC (Fig. 2a) exhibits a stronger inversion consistent with the higher EIS in Fig. 1d. On the other hand, open MCC (Fig. 2b) displays a higher inversion altitude, which is typically associated with conditions favorable for enhanced precipitation[57].

Seasonal variations in the CCN-precipitation relationship

Although we have less than six complete years of all observations, it is of interest to examine the seasonal cycle of these records (Table 3), in an effort to investigate the role of precipitation in this cycle. Turning first to the median baseline N_{CCN}, we observe a strong seasonal cycle with an Austral summer (DJF) maximum of 157 cm^{-3} and a winter (JJA) minimum of 54 cm^{-3}, which is consistent with the long-term CGO records[20,21,28,29,34,37,69,70]. The average baseline precipitation rate and frequency exhibit a pattern opposite to that of median N_{CCN}, with a maximum in winter (2.69 mm day^{-1} occurring 20.3% of the time) and a minimum in summer (0.68 mm day^{-1} occurring 6.4% of time). We note that the average baseline precipitation rate (1.69 mm day^{-1}) substantially contributes to the overall precipitation rate across this latitude band (2.5–3.2 mm day^{-1})[48], which is found in various precipitation products[48]. Statistical independent sample

Table 3 | Seasonal variations

Season (No. of hours in baseline)	Frequency of coverage (%)	Median N_{CCN} (5th, 95th)	Precipitation rate (mm day^{-1})	Precipitation frequency (%)
Annual (17470) All Baseline	–	87 (23, 248)	1.69	13.6
Summer (4394) All Baseline	–	157 (52, 327)	0.68	6.4
Autumn (4462) All Baseline	–	81 (23, 201)	1.95	15.4
Winter (3836) All Baseline	–	54 (16, 127)	2.69	20.3
Spring (4778) All Baseline	–	84 (24, 203)	1.58	13.1
Annual Open MCC	18.8	69 (23, 174)	1.72	16.7
Summer Open MCC	6.2	145 (72, 241)	1.07	12.4
Autumn Open MCC	14.3	78 (32, 160)	1.97	17.2
Winter Open MCC	30.7	47 (18, 115)	1.77	18.9
Spring Open MCC	25.0	75 (26, 174)	1.68	15.2
Annual Closed MCC	6.0	89 (34, 222)	0.29	4.5
Summer Closed MCC	4.8	165 (76, 271)	0.10	2.9
Autumn Closed MCC	8.3	90 (36, 189)	0.44	6.5
Winter Closed MCC	5.2	64 (29, 125)	0.33	4.5
Spring Closed MCC	5.6	86 (32,171)	0.16	3.0

Median N_{CCN}, mean precipitation rate and frequency across all baseline conditions regardless of MCC type and also for the open and closed MCC cases within the 100 km radiuses and 3 h averaging time and the FC_{MCC} threshold of 80% for 2016–2021 along with the frequency of their presence.

tests, including two-tailed Student's t test and Whitney U test, were conducted to assess the significance of the observed differences in N_{CCN} and precipitation. These tests aimed to test the null hypotheses that there is no difference in N_{CCN} and precipitation across the seasons. The results confirmed that these differences are statistically significant ($p < 0.05$), reinforcing the validity of our findings.

After segregating the records into open and closed MCC cases, we observe an inverse tendency between N_{CCN} and precipitation when we analyze the data across different seasons (except for the closed MCC during the winter, which can be attributed to the limited number of cases with precipitation from closed MCC during this season). Further we find that for all seasons, open MCC has a greater average precipitation rate where it is more frequent as well and lower median N_{CCN} compared to closed MCC (Table 3). The relative difference in median N_{CCN} is least in summer (12%) and greatest in winter (27%). The most pristine air is observed at CGO when open MCC is present upwind during the winter season. Using the statistical tests (including two-tailed Student's t test and Whitney U test), we tested the null hypotheses that there is no difference in N_{CCN} and precipitation between open and closed MCC across different seasons, which confirm the significance of these differences ($p < 0.05$).

We further note a strong seasonal cycle in the frequency of coverage of open MCC with a wintertime peak of 30.7% of all baseline records and a summertime minimum of 6.2% (Table 3). Such a seasonal cycle is consistent with numerous climatological studies (e.g.[60,68]). Conversely no substantial seasonal cycle is evident in the frequency of occurrence of closed MCC (Table 3).

Using HYSPLIT back trajectories we sought to establish whether differences in the air mass origin could be linked to differences in N_{CCN}, and potentially cloud morphology. The 72-h back trajectories (Fig. 3), however, are not conclusive with only weak differences between seasons and between the open and closed MCC. Immediately upwind of Tasmania, back trajectories of closed MCC predominantly come from the west, while open MCC trajectories have mostly a south-westerly origin. During winter, open MCC back trajectories tend to originate at higher latitudes than closed MCC. Also, for closed MCC during winter, there is an interesting air mass origin region in the Australian Bight, near the coast. The average N_{CCN} for these scenes was similar to overall average. In general, the baseline air masses originate from higher latitudes, as previously established. Only rarely do these back trajectories cross over Antarctica. The vertical component of these back trajectories (Fig. 4) suggests that large-scale subsidence prevails for both open and closed MCC, somewhat stronger for closed MCC. Back trajectories of open MCC in winter show considerably more spread through the boundary layer, suggesting a well-mixed boundary layer due possibly to active shallow convection. There is less spread in the vertical history of closed MCC back trajectories, consistent with widespread subsidence.

An alternate hypothesis for the cause of the observed seasonal cycle in open MCC and precipitation at CGO pertains to the annual migration in the subtropical ridge, which reaches its highest latitude (38° S) along Australia during February with an average intensity of 1016 hPa[71]. During winter the subtropical ridge strengthens in intensity but retreats to lower latitudes (28° S) over the Australian continent. Manton et al.[48] found a strong correlation coefficient (~−0.6) between precipitation and MSLP across the SO, highlighting the importance of the general circulation in precipitation processes.

The seasonal cycles of atmospheric stability parameters were analyzed (Table 4) to further assess their relationship to the baseline conditions and cloud morphology. These parameters are important for determining the depth of the MABL and evolution of low clouds[61], which are a major source of precipitation in many regions. Lang et al.[72] also found a connection between EIS and the occurrence of precipitation over Macquarie Island. Both M and EIS show a seasonal cycle with stronger stability (lower M and higher EIS) during summer (DJF), consistent with Lang et al.[72] and McCoy et al.[61]. Also, there is a stronger inversion (61% greater EIS) under closed MCC coverage, consistent with the composite sounding (Fig. 2a). Thus, these meteorological controls may be of further importance in setting the seasonal cycle of precipitation, which may also contribute to the seasonal cycle of N_{CCN}.

In order to evaluate the importance of wet deposition in the evolution of the CCN budget from closed to open MCC across the SO, we sought to employ a quantitative approach. Previous studies have noted the importance of precipitation in the transition from closed to open MCC[64,66,73] and the hypothesis is that wet deposition will clean out the MABL by removing particles. Kang et al.[43] utilized the recent summertime Clouds Radiation Aerosol Transport Experimental Study (SOCRATES) campaign over the SO to drive the CCN budget model developed by Wood et al.[42]. This model considers various source and sink terms, including entrainment of CCN from the free troposphere (N_{FT}), primary production at the sea surface from sea-spray (N_s) and precipitation that is induced by coalescence scavenging (N_p)[7,42,43]. Kang et al.[43] assumed the system was at steady state and found that

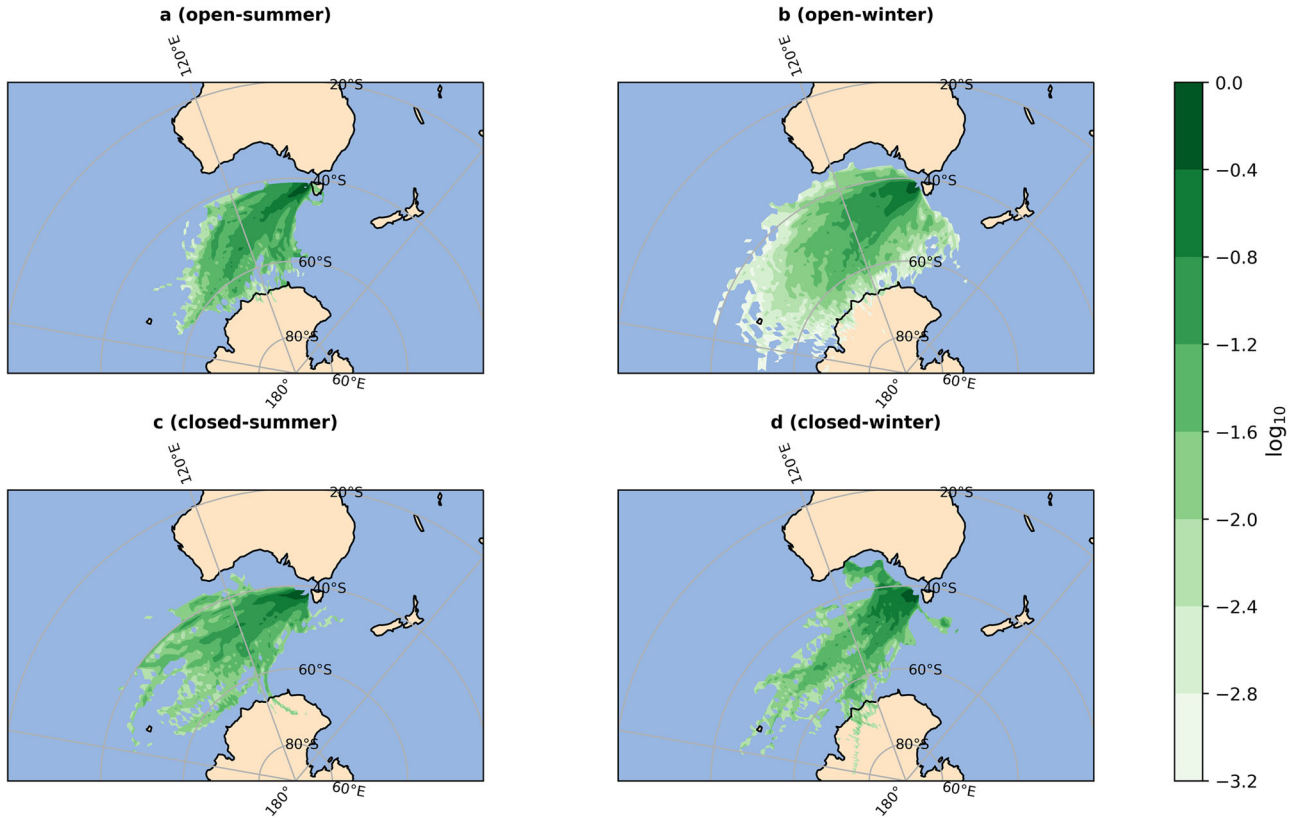


Fig. 3 | Air masses origin. Back trajectories of air parcels at a height of 1000 m at Kennaook/Cape Grim for a 72-h period, during Austral summer (left) and winter (right) when more than 80% of the baseline with a radius of 100 km was covered by open MCC (top) and closed MCC (bottom) for 3 h averaging time (2016–2021).

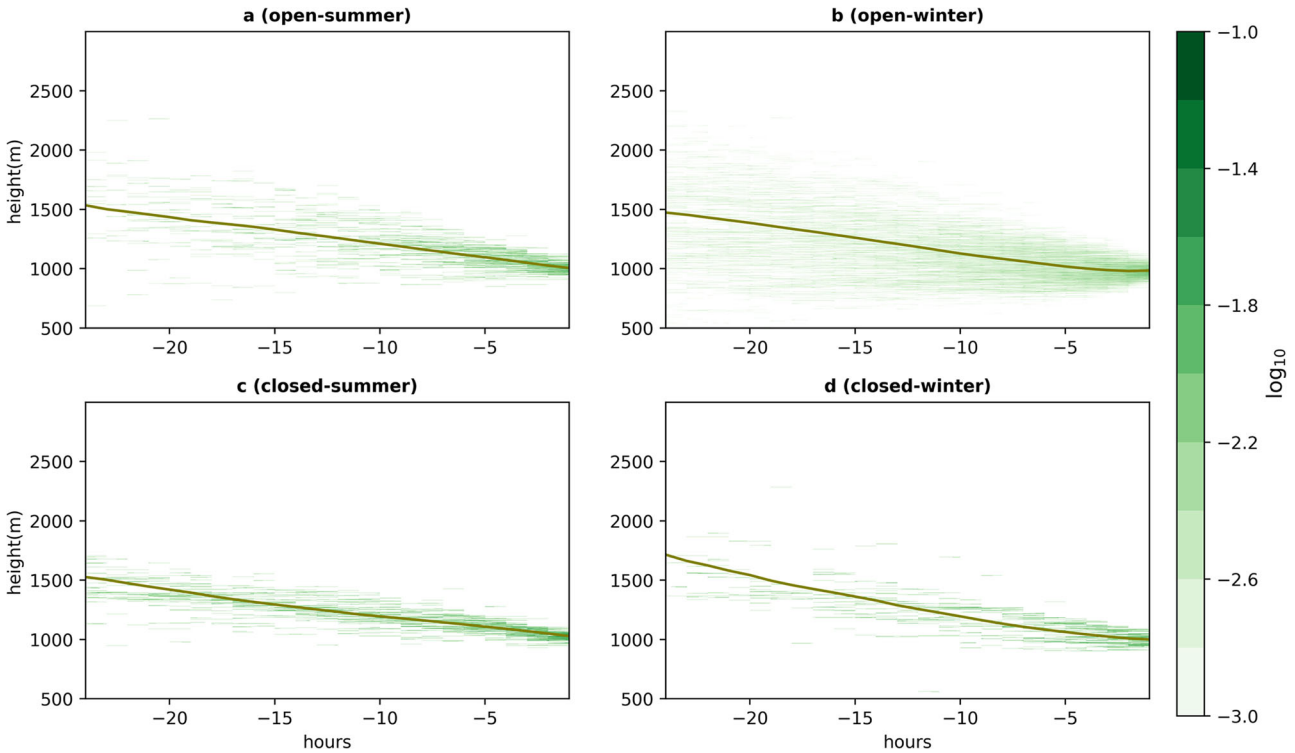


Fig. 4 | Back trajectory altitude. Vertical motion along the average back trajectory (solid line) of the 24-h back trajectories of air parcels at a height of 1000 m, for cases where more than 80% of the baseline with a radius of 100 km in 3 h averaging time, was covered by open MCC (top) and closed MCC (bottom) for Austral summer (left) and winter (right) (2016–2021).

Table 4 | Seasonal variations for meteorological parameters

Season (No. of hours in baseline)	*M*	EIS	MSLP (hPa)
Summer (4394) All Baseline	−3.66	6.26	1012.9
Autumn (4462) All Baseline	−0.69	5.85	1016.9
Winter (3836) All Baseline	0.20	4.26	1016.6
Spring (4778) All Baseline	−1.48	5.29	1015.1
Summer Open MCC	1.94	2.73	1010.5
Autumn Open MCC	2.24	3.69	1014.8
Winter Open MCC	1.30	3.27	1015.7
Spring Open MCC	0.98	3.29	1014.1
Summer Closed MCC	−3.95	8.43	1014.8
Autumn Closed MCC	0.77	9.28	1019.8
Winter Closed MCC	0.27	7.40	1024.0
Spring Closed MCC	−1.38	8.66	1019.9

Average MSLP, M and EIS of the whole baseline followed with the open and closed condition considering the cases for the 100 km radiuses and 3 h averaging time and the FC_{MCC} threshold of 80%.

the CCN budget was most sensitive to the N_{CCN} of the overlying free troposphere compared to other sources. Coalescence scavenging was also found to be an important sink.

Following Kang et al.[43], we also employed the CCN budget model along with available datasets to perform a CCN budget analysis. Considering the relatively constant N_{FT} and N_s during the summer when moving between open and closed MCC (as suggested by Kang et al.[43]), we can assume that

$$\frac{N_{closed} - N_{open}}{\Delta t} = \dot{N}_{pclosed} - \dot{N}_{popen} \quad (1)$$

This equation suggests that the reduction in N_{CCN} from closed to open MCC can be attributed to precipitation along the trajectory. The precipitation sink term depends upon the following terms[74]:

$$\dot{N}_P = K\, N\, P_{CB} h / z_i \quad (2)$$

where P_{CB} represents the precipitation rate at cloud base, $K = 2.25\ m^2\ kg^{-1}$ is a constant that depends on the collection efficiency of cloud droplets by drizzle drops, h is the cloud thickness and z_i is the depth of the MABL[74]. Due to the lack of cloud base precipitation measurements in our datasets, we use surface precipitation data as a proxy for P_{CB}. Cloud thickness and boundary layer height are estimated using the composite ERA5 soundings.

Our calculations indicate that it would take approximately 3 h for precipitation during the transition from closed to open MCC to remove the 12% median CCN differences between closed ($165\ cm^{-3}$) and open MCC ($145\ cm^{-3}$) during summer. It should be noted that this estimate is defined by constraints in our calculation. Extending such quantitative analysis to other seasons is limited by a lack of enough observational information (e.g., the N_{FT} and N_s). Nonetheless, our expanded budget analysis for other seasons indicates transition time within the range of 2–6 h. Another limitation of this analysis pertains to the estimation of precipitation that is induced by coalescence scavenging (N_p), which relies on the precipitation rate at the cloud base level[74]. Our measurements, however, are only available at the surface. Recent research by Kang et al.[75], found substantial differences between precipitation rates at the cloud base and the surface for MABL clouds over the SO using in situ and airborne cloud radar observations. K, which has been used in estimating N_P, is also subject to uncertainty. Nevertheless, these limitations highlight the significance of future coordinated efforts, such as multi-platform measurement campaigns in this region to supply critical datasets needed for cloud-aerosol-precipitation research, including a more comprehensive CCN budget analysis.

Meteorological influences on diurnal precipitation

Moving beyond the seasonal cycle, we can also explore potential relationships between the median N_{CCN} and precipitation at the diurnal time scale, aiming to understand whether CCN acts as the driver of the precipitation, or vice versa. We limit this analysis to the summer season, when solar forcing is most intense and can readily decouple, thin and even completely burn off MABL clouds[76,77]. The Lang et al.[68] cloud climatology readily found such a diurnal cycle in closed MCC over the latitude band between 40° to 50° south. For this analysis, however, we employ all baseline samples (open, closed and other) to increase the sample size and ensure a sufficient amount of data for analysis and to clearly illustrate the diurnal cycle. Furthermore, in order to adequately assess the diurnal cycle, data for precipitation and N_{CCN} from 2011 to 2015 has been included in this analysis (both data were not available before 2011). Looking first at the precipitation (Fig. 5b, c), a strong diurnal cycle is evident in both mean precipitation rate and frequency with a peak in the early morning (5 AM local time) and a minimum in the afternoon. It should be mentioned that the 25th and 75th percentile of precipitation were not presented as both values were zero during the summer. Lang et al.[72] and Tansey et al.[58] found a similar diurnal cycle in precipitation over Macquarie Island. The median N_{CCN} at CGO (Fig. 5a) also displays a diurnal cycle, contrasting with the precipitation pattern with a peak concentration observed at 8 PM. Ayers and Gillet[20] and Ayers et al.[69] also found a diurnal cycle for N_{CCN} over the CGO. Wider research suggests that the thinning of the marine boundary layer clouds through solar forcing/burn off is likely to be driving the diurnal cycle of the precipitation rate[72,78]. Additionally, we observe a diurnal cycle in MSLP (Fig. 5d) and the two stability parameters (M and EIS) (Fig. 5e, f). These meteorological conditions, particularly the stability of the atmosphere and related dynamics, are likely other drivers of the observed diurnal cycles in precipitation. It is especially intriguing to note that the minimum of MSLP coincided with the peaks of precipitation frequency and intensity. These findings further emphasize the crucial role of meteorological controls on ACPI.

In our effort to examine the meteorological impacts on ACPI behaviors, we employed multilinear regression to examine the relationship between meteorological factors, precipitation and aerosol. Subsequently, we removed the meteorological influences on precipitation and N_{CCN} and examined the residuals. Notably, our findings indicate that, after controlling for the meteorology, the correlation between precipitation and N_{CCN} decreased from −0.045 to −0.034 (see details in the attached supplementary materials), suggesting that a substantial portion of the relationship between precipitation and CCN is explained by meteorological factors. Additionally, we conducted a comprehensive analysis comparing multilinear regression models of precipitation with and without considering CCN, revealing minimal differences in R^2 values and correlation coefficients (see details in the attached supplementary materials). This underscores the limited influence of CCN on precipitation, emphasizing the substantial role played by meteorological factors in shaping their relationship. It is important to note that our findings do not imply that the role of CCN is negligible, especially in a changing climate. Even minor influences from the CCN could have important effects on climate given the complexity of the climate system.

Importantly we note that the diurnal cycle in precipitation leads the small diurnal cycle in CCN by roughly 3 h (Fig. 5). To test the significance of this time lag, we applied the Bootstrapping method by which 10000 samples were randomly drawn with a sample size of 8000 (from a total of 8200-time steps). The results indicate that in over 98% of the instances, the minimum N_{CCN} occurred after the maximum precipitation (in just 2% of the instances, the minimum N_{CCN} preceded the maximum precipitation). This suggests that the diurnal cycle in precipitation is unlikely to be led by CCN (with a confidence level of 98%). These analyses emphasize that multiple factors, particularly the meteorology, are likely at play in shaping the diurnal patterns of precipitation, and the influence of CCN on precipitation is not a dominant mechanism over our study area. Again, further investigation is needed to explore how precipitation may be influencing the diurnal cycle of CCN through processes like wet deposition, but it is clear that the relationship between CCN and precipitation is complex.

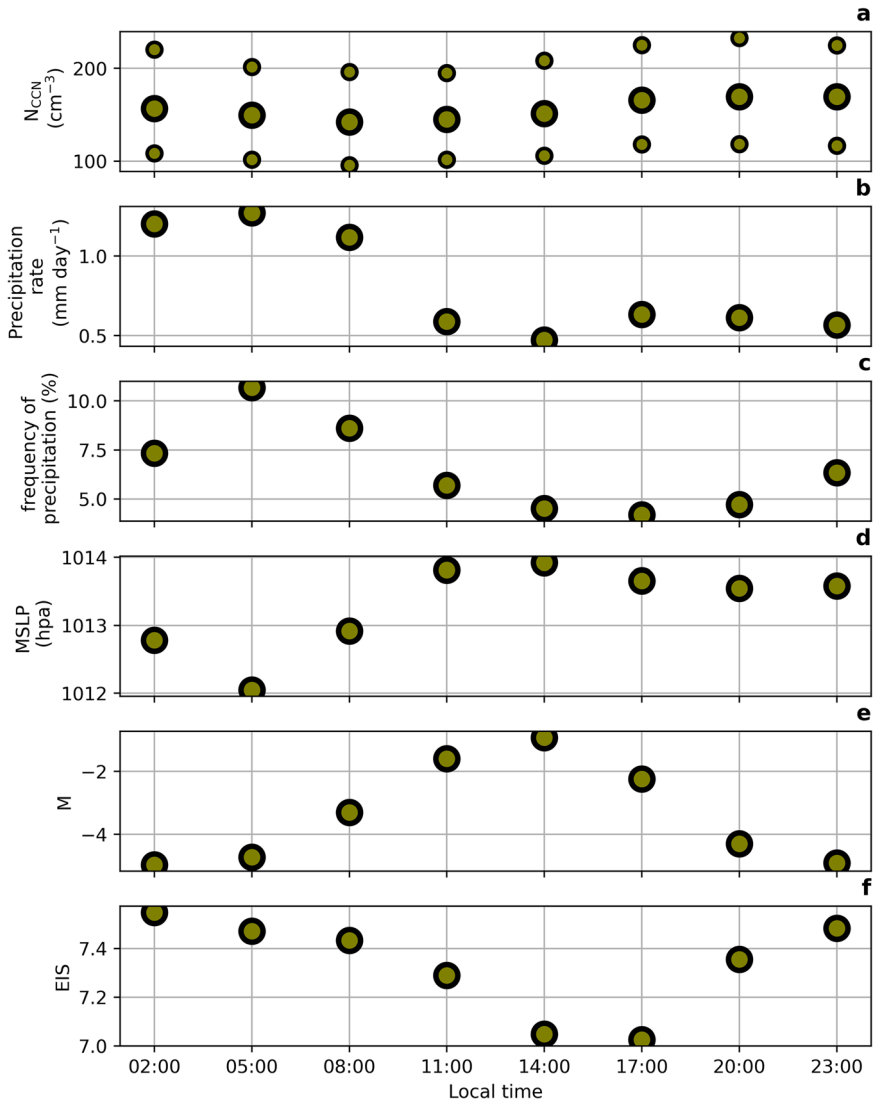


Fig. 5 | Diurnal variations. Diurnal cycle of N_{CCN} (cm^{-3}) (median followed by 25th and 75th percentile) (**a**), average precipitation rate (mm day^{-1}) (**b**) and frequency of precipitation (%) (**c**), MSLP (**d**), M (**e**) and EIS (**f**) during the summertime (2011–2021) in baseline of CGO.

Overall, this analysis once again suggests that a greater understanding of the sinks of aerosols is required to more accurately close the CCN budget across the SO. Specifically, this analysis highlights the potential importance of precipitation in this regard, and the role of the large-scale circulation in driving precipitation across this region.

Methods

Data

The Baseline Air Pollution Monitoring (BAPMon) Station at Kennaook/Cape Grim (CGO) began operations in 1976 as part of the World Meteorological Organization BAPMon program of global atmospheric composition measurements relevant to climate. The observatory is situated at 40° 40′ 56″ S, 144° 41′ 18″ E, at the north-west tip of Tasmania, to ensure observations of SO air with minimal anthropogenic influences. The observatory building is located 94 m above sea level, roughly 100 m inland from the coastline break[20,37,70]. Figure 6 depicts the location of Cape Grim.

The N_{CCN} for particles active at several supersaturations, but predominantly at 0.5% supersaturation (other supersaturations are not available hourly), was determined using a continuous-flow, streamwise thermal gradient CCN counter (CCNC, model CCN-100, Droplet Measurement Technologies, Longmont, CO, USA)[70]. The CCN counter supersaturation was calibrated annually using monodisperse ammonium sulfate particles[37]. The hourly N_{CCN} over CGO for 11 years (2011–2021) was used to examine the role of precipitation and cloud morphology on SO N_{CCN}. The data are available in the World Data Centre for Aerosols (http://www.gaw-wdca.org/).

However, it should be noted that 5 months of CCN records were lost during a COVID lockdown (from the end of September 2020 to March 2021) when the instrument was non-operational. The hourly precipitation data, expressed as mm day^{-1}, were from the Australian Bureau of Meteorology rain gauge at CGO (Station ID: 091331) for the same period of time.

The measurement of radon is also carried out hourly with the dual-flow-loop two-filter atmospheric radon detectors over the CGO station[79,80]. With its predominantly terrestrial source, unreactive nature, and 3.82-day radioactive half-life, radon is an unambiguous tracer of terrestrial influences on sampled air masses[81–83]. The fifth generation of European ReAnalysis (ERA5) wind data, produced by the European Centre for Medium-Range Weather Forecasts (ECMWF)[84], which is available through the Copernicus Climate Change Service Climate Data Store (https://cds.climate.copernicus.eu), were used along with the radon to determine baseline conditions for the same time period.

Finally, the hourly climatology of open and closed MCC is calculated from Himawari-8 imagery (13 μm channel) using a hybrid convolutional neural network (for more details, see Lang et al.[68]) for the six years (2016–2021). Himawari-8, a geostationary meteorological satellite, was launched by the Japanese Meteorological Agency in July 2015 and covers a large part of the SO[85]. The classification of MCC into open and closed categories was not based on cloud fraction or liquid water content, but rather relied on a convolutional neural network's pattern recognition capabilities, as demonstrated by Lang et al.[68]. They constructed and trained it to identify

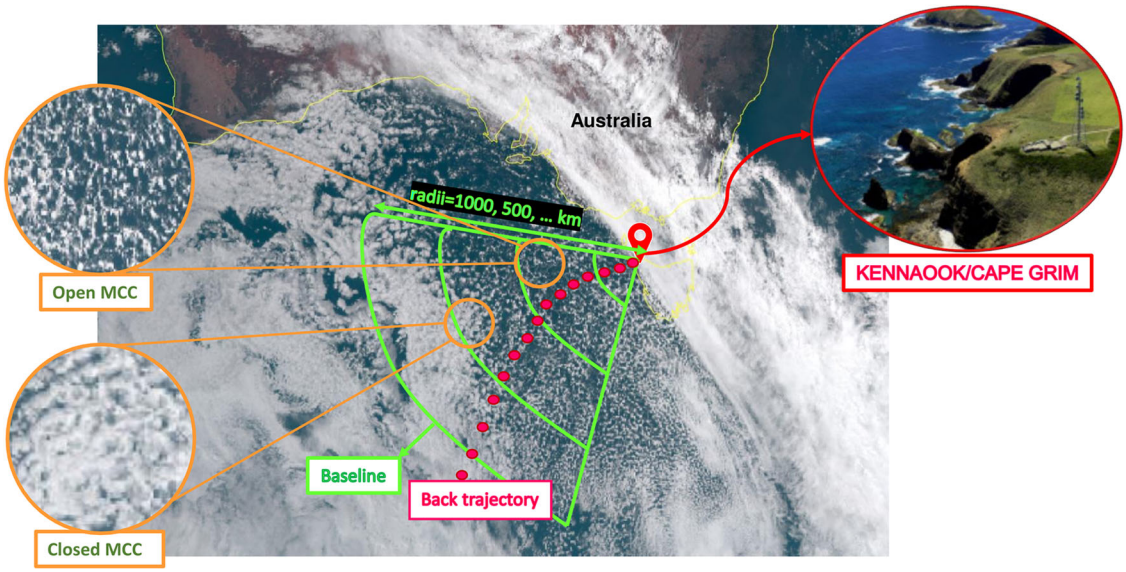


Fig. 6 | Overview of the study area and methodology. A true colour image of Himawari-8 (https://www.eorc.jaxa.jp/ptree/) on 14 January 2016, 00:00 UTC, supplied by the P-Tree System, Japan Aerospace Exploration Agency (JAXA), which illustrates the study area (CGO image sourced from https://capegrim.csiro.au/), the baseline sector defined based on different radii in green colour, symbolizing the varying analysis areas, a sample back trajectory in red colour started from CGO and also a snapshot of different upwind cloud morphologies.

highly ideal open and closed MCC imagery. All other scenes (e.g., clear sky, frontal clouds, cirrus clouds, stratus, disorganized MCC) are simply grouped together as "other" which restricts the ability to examine these circumstances. It should be noted that our analysis is limited by the availability of Himawari-8 records, which became operational in July 2015[85], for classifying the cloud morphology at the time of writing.

Methodology

The initial hypothesis was evaluated using these datasets with two different methodologies. The first method defines baseline conditions, as local wind directions between 190 between 280 degrees (e.g.[37,86]) and ambient radon concentration less than 150 mBq m^{-3}, which includes approximately 80% of baseline sector observations[37]. To assess the sensitivity of the analysis to radon concentration thresholds, we also tested a lower threshold of 100 mBq m^{-3}. Qualitatively, the results are not sensitive to different radon concentration thresholds. Air sampled in the 'baseline' sector (190°–280°) frequently traveled thousands of kilometres across the SO since last land contact. Baseline sector and other detailed parameters for this method are depicted in Fig. 6 (green colours) and will be discussed later. The second method was based on back-trajectory calculations made with the Hybrid Single Particle Lagrangian Integrated Trajectory (HYSPLIT) model[87] employing ERA5 meteorological data, providing the transit history of each air parcel (red colour in Fig. 6). It provided information on the impact of MCC type on each air parcel on its journey to CGO. Back trajectories were started at 1000 m elevation; nevertheless, the results are qualitatively similar to an initial elevation of 500 m. Since the results for both methods are consistent, we employed only the first method. This analysis is limited to 2016–2021 due to the availability of open and closed MCC climatology data from Himawari-8 observations. However, for the diurnal cycle analysis of precipitation and N_{CCN} under baseline conditions, we used the full 11-year dataset to increase the sample size. Cloud morphology is not considered in the diurnal cycle analysis due to the small sample size for the period of summer 2016 to 2021.

Application of the baseline constraints, using ERA5 wind data and the radon constraint, leads to the elimination of 63% of all hourly records. For the remaining 17470 h, the fraction of coverage for both open and closed MCC (FC_{MCC}) was calculated using the Lang et al. classification[68] on Himawari-8 imagery over various upwind averaging times (1, 3 and 6 h) in the baseline sector with various upwind domain radii (50, 100, 200, 300, 500 and 1000 km) as shown in Fig. 6 (green colours). The upwind averaging time accounted for the travel time of air parcels in the baseline sector to reach CGO, while various domain radii were considered to assess the potential influence of upstream frontal systems on the results. For each upwind radius and averaging time, the mean domain FC_{MCC} for both open and closed MCC was computed. The FC_{MCC} is defined as the percentage of the baseline sector covered by either open or closed MCC within the specified radius. To distinguish whether a sample was primarily open or closed MCC, two FC_{MCC} thresholds were used: 50% was considered as a basic requirement while 80% was considered as a more certain requirement. These trials assessed the sensitivity of the results to the upwind radius and upwind averaging time. For each configuration, we considered cases where either open or closed MCC covered more than 50% or 80% of the baseline sector (FC_{MCC} >50% or 80% for open and closed). The median and the 5th and 95th percentiles of N_{CCN} were determined for the times when each cloud class (open or closed MCC) was dominant (FC_{MCC} >50% or 80%). Mean precipitation intensity and frequency were also determined for each case.

To briefly investigate potential meteorological factors influencing the observed cycles in precipitation from open and closed MCCs, we examined the stability parameters including the estimated inversion strength (EIS) and the marine cold air outbreak parameter (M). Each is calculated using ERA5 reanalysis. EIS estimates the strength of the planetary boundary layer inversion and is defined as[88]

$$EIS = LTS - \Gamma_m^{850}(z_{700} - LCL) \quad (3)$$

where the LTS is the lower tropospheric stability defined as the difference in potential temperature between 700 hPa and the surface ($LTS = \theta_{700} - \theta_{surf}$)[89], Γ_m^{850} is the moist-adiabatic potential temperature gradient at 850 hPa, Z_{700} is the altitude of the 700 hPa level and LCL is the lifting condensation level. Greater EIS indicates stronger temperature inversions, which can suppress vertical mixing and reduce the potential for cloud development and precipitation[72,88,90,91]. M was originally defined by Kolstad and Bracegirdle[92] and modified by Fletcher et al.[93] as the difference between the surface skin potential temperature and the 800 hPa potential temperature[93]. However, given that our study area is in the Southern Hemisphere, we used the 850 hPa potential temperature for the M calculation. This is consistent with Papritz et al.[94] over the South Pacific. Moreover, considering the surface skin temperature instead of sea surface temperature will exclude the areas of high

sea-ice cover[93]. Positive M indicates a cold air mass over a relatively warmer surface, leading to an absolutely unstable boundary layer. This condition favours cellular convection, a typical signature of cold air outbreaks, which can result in precipitation[61,93].

HYSPLIT back-trajectories were checked to examine whether any differences between open and closed MCC were linked to airmass origins. Each back-trajectory was run from ERA5 fields for 72 h initiated at a height of 1000 m at CGO. To run the back-trajectories, instances were classified as either open or closed depending on whether the FC_{MCC} for a 100 km upwind length and 3 h averaging time was greater than 80%.

Data availability

The CCN concentration measurement, analyzed during the current study are available in the World Data Centre for Aerosols [http://www.gaw-wdca.org/]. The ECMWF-ERA5 reanalysis datasets are available through the Copernicus Climate Change Service Climate Data Store [https://cds.climate.copernicus.eu]. The precipitation data can be obtained by contacting [climatedata@bom.gov.au]. The radon data is available from the World Data Centre for Greenhouse Gases (WDCGG) [https://gaw.kishou.go.jp/] and from Alastair Williams from Australian Nuclear Science and Technology Organisation (ANSTO). The climatology of open and closed MCC available from the F. Lang on reasonable request.

Code availability

All relevant codes used in this work are not publicly available but can be made available to qualified researchers upon reasonable request from the corresponding author.

Received: 24 April 2023; Accepted: 14 March 2024;
Published online: 22 March 2024

References

1. Uetake, J. et al. Airborne bacteria confirm the pristine nature of the Southern Ocean boundary layer. *Proc. Natl Acad. Sci.* **117**, 13275–13282 (2020).
2. Hudson, J. G., Xie, Y. & Yum, S. S. Vertical distributions of cloud condensation nuclei spectra over the summertime Southern Ocean. *J. Geophys. Res.: Atmos.* **103**, 16609–16624 (1998).
3. Mace, G. G. et al. A description of hydrometeor layer occurrence statistics derived from the first year of merged Cloudsat and CALIPSO data. *J. Geophys. Res.: Atmos.* **114**, D00A26 (2009).
4. Ellis, T. D., L'Ecuyer, T., Haynes, J. M. & Stephens, G. L. How often does it rain over the global oceans? The perspective from CloudSat. *Geophys. Res. Lett.* **36**, L03815 (2009).
5. Hamilton, D. S. et al. Occurrence of pristine aerosol environments on a polluted planet. *Proc. Natl Acad. Sci.* **111**, 18466–18471 (2014).
6. Carslaw, K. S. et al. Aerosols in the pre-industrial atmosphere. *Curr. Clim. Change Rep.* **3**, 1–15 (2017).
7. McCoy, I. L. et al. The hemispheric contrast in cloud microphysical properties constrains aerosol forcing. *Proc. Natl Acad. Sci.* **117**, 18998–19006 (2020).
8. Trenberth, K. E. & Fasullo, J. T. Simulation of present-day and twenty-first-century energy budgets of the southern oceans. *J. Clim.* **23**, 440–454 (2010).
9. Bodas-Salcedo, A. et al. Origins of the solar radiation biases over the Southern Ocean in CFMIP2 models. *J. Clim.* **27**, 41–56 (2014).
10. Kay, J. E. et al. Global climate impacts of fixing the Southern Ocean shortwave radiation bias in the Community Earth System Model (CESM). *J. Clim.* **29**, 4617–4636 (2016).
11. Zelinka, M. D. et al. Causes of higher climate sensitivity in CMIP6 models. *Geophys. Res. Lett.* **47**, e2019GL085782 (2020).
12. Schuddeboom, A. J. & McDonald, A. J. The Southern Ocean radiative bias, cloud compensating errors, and equilibrium climate sensitivity in CMIP6 models. *J. Geophys. Res.: Atmos.* **126**, e2021JD035310 (2021).
13. Fiddes, S. L., Protat, A., Mallet, M. D., Alexander, S. P. & Woodhouse, M. T. Southern Ocean cloud and shortwave radiation biases in a nudged climate model simulation: does the model ever get it right? *Atmos. Chem. Phys.* **22**, 14603–14630 (2022).
14. Bellouin, N. et al. Bounding global aerosol radiative forcing of climate change. *Rev. Geophysics* **58**, e2019RG000660 (2020).
15. Mace, G. G. & Protat, A. Clouds over the Southern Ocean as observed from the R/V Investigator during CAPRICORN. Part I: Cloud occurrence and phase partitioning. *J. Appl. Meteorol. Climatol.* **57**, 1783–1803 (2018).
16. Schmale, J. et al. Overview of the Antarctic circumnavigation expedition: Study of preindustrial-like aerosols and their climate effects (ACE-SPACE). *Bull. Am. Meteorol. Soc.* **100**, 2260–2283 (2019).
17. McFarquhar, G. M. et al. Observations of clouds, aerosols, precipitation, and surface radiation over the Southern Ocean: an overview of CAPRICORN, MARCUS, MICRE and SOCRATES. *Bull. Am. Meteorological Soc.* **102**, E894–E928 (2020).
18. Lohmann, U. & Feichter, J. Global indirect aerosol effects: a review. *Atmos. Chem. Phys.* **5**, 715–737 (2005).
19. Charlson, R. J., Lovelock, J. E., Andreae, M. O. & Warren, S. G. Oceanic phytoplankton, atmospheric sulphur, cloud albedo and climate. *Nature* **326**, 655–661 (1987).
20. Ayers, G. & Gillett, R. DMS and its oxidation products in the remote marine atmosphere: implications for climate and atmospheric chemistry. *J. Sea Res.* **43**, 275–286 (2000).
21. Ayers, G. P. & Cainey, J. M. The CLAW hypothesis: a review of the major developments. *Environ. Chem.* **4**, 366–374 (2007).
22. McCoy, D. T. et al. Natural aerosols explain seasonal and spatial patterns of Southern Ocean cloud albedo. *Sci. Adv.* **1**, e1500157 (2015).
23. Boers, R., Ayers, G. & GRAS, L. J. Coherence between seasonal variation in satellite-derived cloud optical depth and boundary layer CCN concentrations at a mid-latitude Southern Hemisphere station. *Tellus B* **46**, 123–131 (1994).
24. Boers, R. Influence of seasonal variation in cloud condensation nuclei, drizzle, and solar radiation, on marine stratocumulus optical depth. *Tellus B: Chem. Phys. Meteorol.* **47**, 578–586 (1995).
25. Boers, R., Jensen, J., Krummel, P. & Gerber, H. Microphysical and short-wave radiative structure of wintertime stratocumulus clouds over the Southern Ocean. *Q. J. R. Meteorol. Soc.* **122**, 1307–1339 (1996).
26. Ayers, G. P., Cainey, J. M., Gillett, R. & Ivey, J. P. Atmospheric sulphur and cloud condensation nuclei in marine air in the Southern Hemisphere. *Philos. Trans. R. Soc. Lond. Ser. B: Biol. Sci.* **352**, 203–211 (1997).
27. Boers, R., Jensen, J. & Krummel, P. Microphysical and short-wave radiative structure of stratocumulus clouds over the Southern Ocean: Summer results and seasonal differences. *Q. J. R. Meteorol. Soc.* **124**, 151–168 (1998).
28. Quinn, P. K. & Bates, T. S. The case against climate regulation via oceanic phytoplankton sulphur emissions. *Nature* **480**, 51–56 (2011).
29. Ayers, G. & Gras, J. Seasonal relationship between cloud condensation nuclei and aerosol methanesulphonate in marine air. *Nature* **353**, 834–835 (1991).
30. Leck, C. & Keith Bigg, E. Comparison of sources and nature of the tropical aerosol with the summer high Arctic aerosol. *Tellus B: Chem. Phys. Meteorol.* **60**, 118–126 (2008).
31. Woodcock, A. H. Salt nuclei in marine air as a function of altitude and wind force. *J. Meteorol.* **10**, 362–371 (1953).
32. Woodcock, A. H. & Gifford, M. M. Sampling atmospheric sea-salt nuclei over the ocean. *J. Mar. Res.* **8**, 177–197 (1949).
33. Woodcock, A. H. & Blanchard, D. C. Tests of the salt-nuclei hypothesis of rain formation. *Tellus* **7**, 437–448 (1955).

34. Vallina, S. M., Simó, R. & Gassó, S. What controls CCN seasonality in the Southern Ocean? A statistical analysis based on satellite-derived chlorophyll and CCN and model-estimated OH radical and rainfall. *Glob. Biogeochem. Cycles* **20**, GB1014 (2006).
35. Chubb, T. et al. Observations of high droplet number concentrations in Southern Ocean boundary layer clouds. *Atmos. Chem. Phys.* **16**, 971–987 (2016).
36. Quinn, P., Coffman, D., Johnson, J., Upchurch, L. & Bates, T. Small fraction of marine cloud condensation nuclei made up of sea spray aerosol. *Nat. Geosci.* **10**, 674–679 (2017).
37. Gras, J. L. & Keywood, M. Cloud condensation nuclei over the Southern Ocean: wind dependence and seasonal cycles. *Atmos. Chem. Phys.* **17**, 4419–4432 (2017).
38. Zhang, J. & Feingold, G. Distinct regional meteorological influences on low-cloud albedo susceptibility over global marine stratocumulus regions. *Atmos. Chem. Phys.* **23**, 1073–1090 (2023).
39. Christensen, M. W. et al. Opportunistic experiments to constrain aerosol effective radiative forcing. *Atmos. Chem. Phys. Discuss.* **22**, 641–674 (2022).
40. Wall, C. J. et al. Assessing effective radiative forcing from aerosol-cloud interactions over the global ocean. *Proc. Natl Acad. Sci.* **119**, e2210481119 (2022).
41. Feingold, G., Kreidenweis, S. M., Stevens, B. & Cotton, W. Numerical simulations of stratocumulus processing of cloud condensation nuclei through collision-coalescence. *J. Geophys. Res.: Atmos.* **101**, 21391–21402 (1996).
42. Wood, R., Leon, D., Lebsock, M., Snider, J. & Clarke, A. D. Precipitation driving of droplet concentration variability in marine low clouds. *J. Geophys. Res.: Atmos.* **117**, D19210 (2012).
43. Kang, L., Marchand, R., Wood, R. & McCoy, I. L. Coalescence scavenging drives droplet number concentration in Southern Ocean low clouds. *Geophys. Res. Lett.* **49**, e2022GL097819 (2022).
44. Tornow, F., Ackerman, A. S. & Fridlind, A. M. Preconditioning of overcast-to-broken cloud transitions by riming in marine cold air outbreaks. *Atmos. Chem. Phys.* **21**, 12049–12067 (2021).
45. Yum, S. S. & Hudson, J. G. Wintertime/summertime contrasts of cloud condensation nuclei and cloud microphysics over the Southern Ocean. *J. Geophys. Res.: Atmos.* **109**, D06204 (2004).
46. Ahn, E. et al. In situ observations of wintertime low-altitude clouds over the Southern Ocean. *Q. J. R. Meteorol. Soc.* **143**, 1381–1394 (2017).
47. Bennartz, R. Global assessment of marine boundary layer cloud droplet number concentration from satellite. *J. Geophys. Res.: Atmos.* **112**, D02201 (2007).
48. Manton, M., Huang, Y. & Siems, S. Variations in precipitation across the Southern Ocean. *J. Clim.* **33**, 10653–10670 (2020).
49. Behrangi, A. & Song, Y. A new estimate for oceanic precipitation amount and distribution using complementary precipitation observations from space and comparison with GPCP. *Environ. Res. Lett.* **15**, 124042 (2020).
50. Siems, S. T., Huang, Y. & Manton, M. J. Southern Ocean precipitation: Toward a process-level understanding. *Wiley Interdiscip. Rev.: Clim. Change* **13**, e800 (2022).
51. Montoya Duque, E. et al. A characterization of clouds and precipitation over the Southern Ocean from synoptic to micro scales during the CAPRICORN field campaigns. *J. Geophys. Res.: Atmos.* **127**, e2022JD036796 (2022).
52. Huang, Y., Siems, S. T., Manton, M. J., Hande, L. B. & Haynes, J. M. The structure of low-altitude clouds over the Southern Ocean as seen by CloudSat. *J. Clim.* **25**, 2535–2546 (2012).
53. Huang, Y., Siems, S. T., Manton, M. J., Protat, A. & Delanoë, J. A study on the low-altitude clouds over the Southern Ocean using the DARDAR-MASK. *J. Geophys. Res.: Atmos.* **117**, D18204 (2012).
54. Bodas-Salcedo, A. et al. Large contribution of supercooled liquid clouds to the solar radiation budget of the Southern Ocean. *J. Clim.* **29**, 4213–4228 (2016).
55. Mace, G. G. & Protat, A. Clouds over the Southern Ocean as observed from the R/V Investigator during CAPRICORN. Part II: The properties of nonprecipitating stratocumulus. *J. Appl. Meteorol. Climatol.* **57**, 1805–1823 (2018).
56. Wang, Z., Siems, S. T., Belusic, D., Manton, M. J. & Huang, Y. A climatology of the precipitation over the Southern Ocean as observed at Macquarie Island. *J. Appl. Meteorol. Climatol.* **54**, 2321–2337 (2015).
57. Lang, F., Huang, Y., Siems, S. & Manton, M. Characteristics of the marine atmospheric boundary layer over the Southern Ocean in response to the synoptic forcing. *J. Geophys. Res.: Atmos.* **123**, 7799–7820 (2018).
58. Tansey, E., Marchand, R., Protat, A., Alexander, S. P. & Ding, S. Southern Ocean precipitation characteristics observed from CloudSat and ground instrumentation during the Macquarie Island Cloud & Radiation Experiment (MICRE): April 2016 to March 2017. *J. Geophys. Res.: Atmos.* **127**, e2021JD035370 (2022).
59. Wood, R. & Hartmann, D. L. Spatial variability of liquid water path in marine low cloud: the importance of mesoscale cellular convection. *J. Clim.* **19**, 1748–1764 (2006).
60. Muhlbauer, A., McCoy, I. L. & Wood, R. Climatology of stratocumulus cloud morphologies: microphysical properties and radiative effects. *Atmos. Chem. Phys.* **14**, 6695–6716 (2014).
61. McCoy, I. L., Wood, R. & Fletcher, J. K. Identifying meteorological controls on open and closed mesoscale cellular convection associated with marine cold air outbreaks. *J. Geophys. Res.: Atmos.* **122**, 11,678–11,702 (2017).
62. Wood, R. et al. An aircraft case study of the spatial transition from closed to open mesoscale cellular convection over the Southeast Pacific. *Atmos. Chem. Phys.* **11**, 2341–2370 (2011).
63. Danker, J., Sourdeval, O., McCoy, I. L., Wood, R. & Possner, A. Exploring relations between cloud morphology, cloud phase, and cloud radiative properties in Southern Ocean's stratocumulus clouds. *Atmos. Chem. Phys.* **22**, 10247–10265 (2022).
64. Terai, C., Bretherton, C., Wood, R. & Painter, G. Aircraft observations of aerosol, cloud, precipitation, and boundary layer properties in pockets of open cells over the southeast Pacific. *Atmos. Chem. Phys.* **14**, 8071–8088 (2014).
65. Abel, S. J. et al. Open cells exhibit weaker entrainment of free-tropospheric biomass burning aerosol into the south-east Atlantic boundary layer. *Atmos. Chem. Phys.* **20**, 4059–4084 (2020).
66. Abel, S. J. et al. The role of precipitation in controlling the transition from stratocumulus to cumulus clouds in a Northern Hemisphere cold-air outbreak. *J. Atmos. Sci.* **74**, 2293–2314 (2017).
67. Lang, F. et al. Shallow convection and precipitation over the Southern Ocean: a case study during the CAPRICORN 2016 field campaign. *J. Geophys. Res.: Atmos.* **126**, e2020JD034088 (2021).
68. Lang, F. et al. A climatology of open and closed mesoscale cellular convection over the Southern Ocean derived from Himawari-8 observations. *Atmos. Chem. Phys. Discuss.* **22**, 2135–2152 (2022).
69. Ayers, G., Bentley, S., Ivey, J. & Forgan, B. Dimethylsulfide in marine air at Cape Grim, 41 S. *J. Geophys. Res.: Atmos.* **100**, 21013–21021 (1995).
70. Humphries, R. S. et al. Measurement report: Understanding the seasonal cycle of Southern Ocean aerosols. *Atmos. Chem. Phys.* **23**, 3749–3777 (2023).
71. Larsen, S. H. & Nicholls, N. Southern Australian rainfall and the subtropical ridge: Variations, interrelationships, and trends. *Geophys. Res. Lett.* **36**, L08708 (2009).
72. Lang, F., Huang, Y., Siems, S. T. & Manton, M. J. Evidence of a diurnal cycle in precipitation over the Southern Ocean as observed at Macquarie Island. *Atmosphere* **11**, 181 (2020).

73. Kazil, J. et al. Modeling chemical and aerosol processes in the transition from closed to open cells during VOCALS-REx. *Atmos. Chem. Phys.* **11**, 7491–7514 (2011).
74. Wood, R. Rate of loss of cloud droplets by coalescence in warm clouds. *J. Geophys. Res.* **111**, https://doi.org/10.1029/2006jd007553 (2006).
75. Kang, L., Marchand, R. & Wood, R. Stratocumulus precipitation properties over the Southern Ocean observed from aircraft during the SOCRATES campaign. https://doi.org/10.22541/essoar.169290579.91095731/v1 (2023).
76. Slingo, A., Nicholls, S. & Schmetz, J. Aircraft observations of marine stratocumulus during JASIN. *Q. J. R. Meteorol. Soc.* **108**, 833–856 (1982).
77. Nicholls, S. The dynamics of stratocumulus: aircraft observations and comparisons with a mixed layer model. *Q. J. R. Meteorol. Soc.* **110**, 783–820 (1984).
78. Turton, J. & Nicholls, S. A study of the diurnal variation of stratocumulus using a multiple mixed layer model. *Q. J. R. Meteorol. Soc.* **113**, 969–1009 (1987).
79. Williams, A. & Chambers, S. A history of radon measurements at Cape Grim. *Baseline Atmospheric Program (Australia) History and Recollections, 40th Anniversary Special edn.* 131–146 (2016).
80. Whittlestone, S. & Zahorowski, W. Baseline radon detectors for shipboard use: development and deployment in the First Aerosol Characterization Experiment (ACE 1). *J. Geophys. Res.: Atmos.* **103**, 16743–16751 (1998).
81. Chambers, S. D. et al. Towards a universal "baseline" characterisation of air masses for high-and low-altitude observing stations using Radon-222. *Aerosol Air Qual. Res.* **16**, 885–899 (2016).
82. Chambers, S. D. et al. Characterizing atmospheric transport pathways to Antarctica and the remote Southern Ocean using radon-222. *Front. Earth Sci.* **6**, 190 (2018).
83. Zahorowski, W. et al. Constraining annual and seasonal radon-222 flux density from the Southern Ocean using radon-222 concentrations in the boundary layer at Cape Grim. *Tellus B: Chem. Phys. Meteorol.* **65**, 19622 (2013).
84. Hersbach, H. et al. The ERA5 global reanalysis. *Q. J. R. Meteorol. Soc.* **146**, 1999–2049 (2020).
85. Bessho, K. et al. An Introduction to Himawari-8/9— Japan's New-Generation Geostationary Meteorological Satellites. *J. Meteorol. Soc. Jpn. Ser. II* **94**, 151–183 (2016).
86. Gras, J. Baseline atmospheric condensation nuclei at Cape Grim 1977–1987. *J. Atmos. Chem.* **11**, 89–106 (1990).
87. Draxler, R. R. & Hess, G. D. Description of the HYSPLIT4 modeling system. NOAA Technical Memorandum ERL ARL-224 (1997); https://repository.library.noaa.gov/view/noaa/31133.
88. Wood, R. & Bretherton, C. S. On the relationship between stratiform low cloud cover and lower-tropospheric stability. *J. Clim.* **19**, 6425–6432 (2006).
89. Klein, S. A. & Hartmann, D. L. The seasonal cycle of low stratiform clouds. *J. Clim.* **6**, 1587–1606 (1993).
90. Kubar, T. L., Hartmann, D. L. & Wood, R. Understanding the importance of microphysics and macrophysics for warm rain in marine low clouds. Part I: Satellite observations. *J. Atmos. Sci.* **66**, 2953–2972 (2009).
91. Lamer, K., Naud, C. M. & Booth, J. F. Relationships between precipitation properties and large-scale conditions during subsidence at the Eastern North Atlantic observatory. *J. Geophys. Res.: Atmos.* **125**, e2019JD031848 (2020).
92. Kolstad, E. W. & Bracegirdle, T. J. Marine cold-air outbreaks in the future: an assessment of IPCC AR4 model results for the Northern Hemisphere. *Clim. Dyn.* **30**, 871–885 (2008).
93. Fletcher, J., Mason, S. & Jakob, C. The climatology, meteorology, and boundary layer structure of marine cold air outbreaks in both hemispheres. *J. Clim.* **29**, 1999–2014 (2016).
94. Papritz, L., Pfahl, S., Sodemann, H. & Wernli, H. A climatology of cold air outbreaks and their impact on air–sea heat fluxes in the high-latitude South Pacific. *J. Clim.* **28**, 342–364 (2015).

Acknowledgements

This research has been supported by the Australian Research Council Discovery Projects (DP190101362). Continued support for the Kennaook Cape Grim Program from the Australian Bureau of Meteorology and Commonwealth Scientific and Industrial Research Organisation (CSIRO) is also gratefully acknowledged.

Author contributions

T. Alinejadtabrizi prepared the original draft of the paper and performed most of the data analysis. F. Lang & L. Ackermann prepared the climatology of open and closed MCC for 2016 to 2021. F. Lang also calculated stability parameters over the study area. All co-authors provided editorial feedback on the paper. All co-authors read and approved the final manuscript.

Competing interests

The authors declare no competing interests.

Additional information

Supplementary information The online version contains supplementary material available at https://doi.org/10.1038/s41612-024-00625-1.

Correspondence and requests for materials should be addressed to T. Alinejadtabrizi.

Reprints and permissions information is available at http://www.nature.com/reprints

Publisher's note Springer Nature remains neutral with regard to jurisdictional claims in published maps and institutional affiliations.

Open Access This article is licensed under a Creative Commons Attribution 4.0 International License, which permits use, sharing, adaptation, distribution and reproduction in any medium or format, as long as you give appropriate credit to the original author(s) and the source, provide a link to the Creative Commons licence, and indicate if changes were made. The images or other third party material in this article are included in the article's Creative Commons licence, unless indicated otherwise in a credit line to the material. If material is not included in the article's Creative Commons licence and your intended use is not permitted by statutory regulation or exceeds the permitted use, you will need to obtain permission directly from the copyright holder. To view a copy of this licence, visit http://creativecommons.org/licenses/by/4.0/.

© The Author(s) 2024